Long-period ground motion simulation using centroid moment tensor inversion solutions based on the regional three-dimensional model in the Kanto region, Japan

Shunsuke Takemura (shunsuke@eri.u-tokyo.ac.jp)
Earthquake Research Institute, the University of Tokyo https://orcid.org/0000-0002-7511-3443
Kazuo Yoshimoto
Yokohama City University
Katsuhiko Shiomi
National Research Institute for Earth Science and Disaster Resilience

---

Full paper

Keywords: CMT inversion, Kanto region, Long-period ground motion, 3D numerical simulation

Posted Date: October 24th, 2020

DOI: https://doi.org/10.21203/rs.3.rs-43689/v2

Version of Record: A version of this preprint was published on January 11th, 2021. See the published version at https://doi.org/10.1186/s40623-020-01348-2.

Abstract

We conducted centroid moment tensor (CMT) inversions of moderate (*Mw* 4.5–6.5) earthquakes in the Kanto region, Japan, using a local three-dimensional (3D) model. We then investigated the effects of our 3D CMT solutions on long-period ground motion simulations. Grid search CMT inversions were conducted using displacement seismograms for the periods of 25–100 s. By comparing our 3D CMT solutions with those from the local one-dimensional (1D) catalog, we found that our 3D CMT inversion systematically provides magnitudes smaller than those in the 1D catalog. The *Mw* differences between 3D and 1D catalogs tend to be significant for earthquakes within the oceanic slab. By comparing the ground motion simulations of the 1D and 3D velocity models, we confirmed that the observed *Mw* differences could be explained by the differences in the rigidity structures around the source regions in the two models. The 3D velocity structures (especially oceanic crust and mantle) are important for estimating seismic moments in intraslab earthquakes. The seismic moments directly affect the amplitudes of ground motions. Thus, 3D CMT solutions are essential for precise forward and inverse modeling of long-period ground motion. We also conducted long-period ground motion simulations using our 3D CMT solutions to evaluate the reproducibility of long-period ground motions at stations within the Kanto Basin. The simulations of our 3D CMT solutions well-reproduced observed ground motions for periods longer than 10 s, even at stations within the Kanto Basin. The reproducibility of simulations using our 3D CMT solutions was better than those based on the solutions in the 1D catalog.

Introduction

Long-period ground motions with predominant periods of several to 20 s have often been observed in large sedimentary basins and offshore regions. The duration and amplitude of long-period ground motion is enhanced due to thick low-velocity sediments along the propagation path (e.g., Boore 1999; Furumura et al. 2001, 2008; Olsen et al. 2006; Day et al. 2008; Gomberg 2018; Kaneko et al. 2019). Thus, long-period ground motions can cause severe resonance and damage of large-scale man-made structures, such as high-rise buildings, oil storage tanks, and suspension bridges. The characteristics of long-period ground motions were have been summarized in Koketsu and Miyake (2008). In the Kanto region, Japan, long-period ground motions with predominant periods of 5–10 s have frequently been observed during shallow moderate-to-large earthquakes (e.g., Kinoshita et al. 1992; Miyake and Koketsu 2005; Yoshimoto and Takemura 2014). The propagation feature of long-period ground motion is complicated due to the lateral variations of sedimentary structures within the Kanto Basin (e.g., Koketsu and Kikuchi 2000; Furumura and Hayakawa 2007; Mukai et al. 2018). Long-period ground motion and the structural properties within the Kanto Basin have been studied extensively using observed seismograms and geological surveys to contribute to disaster mitigation in the Tokyo metropolitan area (e.g., Koketsu et al. 2009; Takemura et al. 2015).

Recent advances in numerical simulation codes (e.g., Gokhberg and Fichtner 2016; Maeda et al. 2017) and local/regional three-dimensional (3D) velocity structure models (e.g., Koketsu et al. 2012; Kennett et al. 2013; Stephenson et al. 2017) have enabled the implementation of realistic 3D simulations of long-period ground motion (e.g., Komatitsch 2004; Iwaki et al. 2018; Wirth et al. 2019), and the estimation of structural properties (e.g., Tape et al. 2009; Gao and Shen 2014; Miyoshi et al. 2017). In forward and inverse modeling of long-period ground motion and structural properties along propagation paths, an assumption of a double-couple point source is usually assumed. The centroid moment tensor (CMT) solutions based on displacement for periods longer than 20 s are generally considered robust against structural heterogeneities, compared to first-motion solutions (e.g., Takemura et al. 2016). As such, one-dimensional (1D) velocity models are adopted in local/global CMT inversion systems (e.g., Kubo et al. 2002; Bernardi et al. 2004; Vallée et al. 2011; Ekström et al. 2012); these solutions are typically used in ground motion simulations. However, in regions with strong heterogeneities, such as thick sediments and subducting oceanic plates, focal mechanisms could be incorrectly estimated using conventional 1D CMT methods. To address this issue, the CMT inversion based on Green's functions using the local/regional 3D model has been developed in such regions (e.g., Lee et al. 2013; Hejrani et al. 2017; Okamoto et al. 2018; Takemura et al. 2018b, a, 2019b, 2020; Wang and Zhan 2020; Hejrani and Tkalčić 2020). By using the 3D CMT results of moderate earthquakes along the Nankai Trough, Takemura et al. (2020) demonstrated that the differences in centroid depths and focal mechanisms between 1D and their 3D CMT solutions were significant for offshore earthquakes due to offshore heterogeneities. These differences could affect ground motion simulations (e.g., Takemura et al. 2019c). To achieve precise forward and inverse modeling of long-period ground motions in the Kanto region, where large sedimentary basin and two subducting plates exist, accurate CMT solutions should be required.

In this study, we conduct CMT inversions of moderate earthquakes in the Kanto region using the 3D Green's function dataset. We evaluate differences in source parameters between 1D and 3D CMT solutions. We conduct ground motion simulations using 3D CMT solutions to discuss the effects of CMT solutions on long-period ground motion modeling in the Kanto Basin. To accurately model phases and amplitudes of long-period ground motion, we demonstrate that the adjusted source model should be incorporated in the used 3D model (e.g., 3D CMT solution).

Method

In this study, we used the F-net broadband seismograms of the target earthquakes. At each F-net station (filled triangles in Figure 1), a broadband velocity seismometer (STS-1, STS-2, or STS-2.5) was installed. The health of the sensors is systematically monitored by the National Research Institute for Earth Science and Disaster Resilience (NIED; Okada et al. 2004; Kimura et al. 2015; National Research Institute for Earth Science and Disaster Resilience 2019). Our target was shallow ($\leq$ 50 km) earthquakes with moment magnitudes (*Mw*) between 4.5 and 6.5, listed in the F-net moment tensor (MT) catalog. The F-net 1D velocity structure model has been used in the F-net MT catalog (Fukuyama et al. 1998; Kubo et al. 2002). Target earthquakes (focal mechanisms in Figure 1) occurred within the assumed source grid area (crosses in Figure 2a) between April 2017 and March 2020. Data from the Metropolitan Seismic Observation Network (MeSO-net) for the analyzed period were also available from the NIED website (e.g., Kasahara et al. 2009; Sakai and Hirata 2009). As MeSO-net stations are densely deployed around the

Tokyo metropolitan area (inverse triangles in Figure 1), we also evaluated long-period ground motion in the Kanto Basin using earthquakes that occurred after April 2017.

CMT inversions were conducted using displacement seismograms for the periods of 25–100 s. By using the Open-source Seismic Wave Propagation Code software "OpenSWPC" (Maeda et al. 2017), we numerically evaluated Green's functions in the 3D model. We used the Japan Integrated Velocity Structure Model version 1 (JIVSM; Koketsu et al. 2012) as the 3D velocity structure model for this study. The JIVSM was constructed by combining the results of geological and geophysical surveys around Japan. The structures beneath the bedrock were modeled using regional-scale tomography and gravity data (e.g., Ryoki 1999; Matsubara et al. 2008; Matsubara and Obara 2011). The model construction procedure was described in detail by Koketsu et al. (2009, 2012). The JIVSM has been widely used in the evaluation of ground motion, crustal deformation, and seismic monitoring across Japan (e.g., Guo et al. 2016; Miyazawa 2016; Agata 2020; Oba et al. 2020; Baba et al. 2020). The simulation model covered an area of 600 × 600 × 160 km^3 (blue dashed rectangle in Figure 2a), which was discretized by grid intervals of 0.5 km in the horizontal directions and 0.2 km in the vertical direction. The physical parameters of each layer in the JIVSM are listed in Table 1. For the calculation of 3D Green's functions, the minimum *S*-wave velocity in the solid column was assumed to be 1.5 km/s. Source grids were uniformly distributed at a horizontal interval of 0.1° and vertical interval of 2 km from depth 6 to 60 km. In the calculation of Green's functions, the Küpper wavelet with a duration of 1 s was employed. The "Seismic Analysis Code" (SAC; Goldstein and Snoke 2005; Helffrich et al. 2013) was used to store simulated seismograms and partly conduct the signal processing. In Green's function evaluation, we discarded any source grids that were within the seawater column and stations with epicentral distances equal to or larger than 550 km. Approximately 13,000,000 Green's function SAC files from 49,279 source grids to 15 F-net stations were obtained by conducting 45 reciprocal calculations. Each reciprocal calculation required 247 GB of computer memory and a wall-clock time of 1 h when parallel computing with the 432 cores of the computer system of the Earthquake and Volcano Information Center at the Earthquake Research Institute, University of Tokyo.

We selected F-net stations within epicentral distances between 100 and 400 km from the initial epicenter, obtained from the F-net MT catalog. A set of Green's functions at the source grids, which were located at ± 0.4° from the initial epicenter and distributed at depths between 6 and 60 km, were selected for grid search inversion. To apply band-pass filter and integration stably, we used 10-min F-net velocity seismograms starting 3 min before the origin minute. A 200 s time window for each CMT inversion was adopted. CMT inversions were conducted every 1 s within ±1 min from the origin minute to determine the centroid time. Time shifts, which can correct for travel time differences between the observed and synthetic seismograms at each station, were not permitted during grid search inversion, despite typical 1D MT routines, such as the F-net MT system, enabling time shifts between synthetic and observed seismograms at each station. From the CMT inversions, we obtained seismic moments and focal mechanisms at all possible spatial and temporal source grids. Then, to identify the optimal solution from all the CMT solutions, we evaluated variance reductions (VRs) between the observed and synthetic displacement seismograms for the periods of 25–100 s. A perfect match between the observations and the synthetic results gives a VR of 100 %. The solution with the maximum VR was considered the optimal solution, providing the optimal centroid location, depth, time, focal mechanism, and seismic moment. Other technical details of CMT inversions using a 3D model and the evaluation of Green's functions are described in Takemura et al. (2020).

We conducted forward simulations of ground motion in the Kanto region to investigate the effects of the CMT solutions, based on the 3D model, on long-period (> 5 s) ground motions. A more realistic velocity model, including velocity layers with *Vs* slower than 1.5 km/s, should be used in the simulations of long-period ground motion. As such, the model used in long-period ground motion simulations included all the sedimentary layers of the JIVSM, as listed in Table 1. The model covered an area of 480 × 480 × 100 km^3 (red dotted rectangle in Figure 2a) and was discretized by grid intervals of 0.2 km in the horizontal directions and 0.1 km in the vertical direction. Simulated seismograms were evaluated at the F-net and MeSO-net stations within the calculation region (red dotted rectangle in Figure 2a). The source parameters for Events a, b, and A–C are listed in Table 3. The centroid locations, times, and moment tensors derived from the 3D CMT solutions were used for the listed earthquakes. The source time functions were characterized by the Küpper wavelet, and durations were assumed based on the empirical relationship between seismic moments and rupture durations (Kanamori and Brodsky 2004). Each simulation of long-period ground motion required 1190 GB computer memory and 4 h computation time. Simulations were performed through parallel computing with 64 nodes of the Fujitsu PRIMERGY CX600M1/CX1640M1 (Oakforest-PAC) at the Information Technology Center, University of Tokyo.

Results: 3d Cmt Solutions Of Moderate Earthquakes Beneath Kanto Region

Figures 2b–d show an example of 3D CMT inversion. The optimal solution for the earthquake on June 8, 2017 is a low-angle (22°) thrust faulting at a depth of 48 km, deeper the upper surface (40 km) and close to the oceanic Moho (48 km) of the Pacific Plate. The F-net MT solution for this earthquake had a similar focal mechanism; however, its centroid depth was slightly (2 km) deeper than in our solution (see numbers above focal spheres in Figure 2b). The spatial variation of the VRs at each source grid is illustrated in Figure 2c. The resolution against centroid time is shown in Figure S1. Although the optimal depth was very close to the upper surface of the Pacific Plate, high (> 80 %) VR solutions appeared at a wider depth range (36–56 km). These features are similar to CMT solutions in the Hyuga-nada region, southwest Japan (Figure 4 of Takemura et al. 2020). The centroid depth constraint is also not high for shallow crustal earthquake (Figure S2). The synthetic seismograms of the optimal solution accurately reproduce the observations. We also derived CMT solutions for this earthquake using the periods of 10–100 s (Figure S3). Similar to Hejrani and Tkalčić (2020), we confirmed that broader period analysis is important for constraining centroid depths. However, we employed the period band of 25–100 s for CMT inversions because the optimal solutions were not changed and the maximum VR was smaller than that for the periods of 25–100 s.

We obtained 74 CMT solutions for shallow earthquakes (<50 km) with an *Mw* of 4.2–6.3; Figure 3a illustrates the spatial distribution of these CMT solutions. All parameters for these CMT solutions are available from the data repository site (https://doi.org/10.5281/zenodo.3926884).

The cross-sections of profiles A and B are plotted at the bottom of Figure 3a. It is evident from profile B that many earthquakes occurred just below the upper surface of the Pacific Plate. To validate our CMT solutions, especially in their epicenter locations and depths, we compared them to hypocenter distributions based on temporal ocean bottom seismometers (Ito et al. 2017a, b) covering the area around profile B. We found good agreement. However, these aligned intraslab earthquakes were not confirmed as such in the F-net catalog (Figure 3b). Although the resolution of centroid depth is not very high, 3D CMT inversion was also considered to work well in the Kanto region. The percentages of isotropic, compensated linear vector dipole (CLVD), and double couple (DC) components in both catalogs are detailed in Figure S4. Differences between our results and F-net catalogs could be caused by the differences in the velocity model and moment tensor inversion settings. In the routine F-net system, the isotropic component is not considered.

Differences between 3D CMT and F-net MT catalogs

The F-net solutions of the corresponding earthquakes are also plotted in Figure 3b. The spatial distributions in the two catalogs seem to be similar. To quantitatively evaluate the differences between the 3D CMT solutions in this study and the F-net MT catalogs, we calculated cross-correlation coefficients for *P*-wave radiation patterns (e.g., Kuge and Kawakatsu 1993; Helffrich 1997), depth, and *Mw* differences between the two catalogs (Figure 4). A large negative (−0.6) cross-correlation coefficient only appeared in a solution for an earthquake on February 23, 2019. Only 4 F-net stations (N.JIZF, N.KZKF, N.YMZF, and N.KSKF; see Figure 2b) were applicable for CMT inversion of this earthquake because of low signal-to-noise ratios (SNR) in the 25–100 s periods. Additionally, the VR of the 3D CMT solution was not high (~57 %). With the exception of this event, the differences in focal mechanisms and centroid depths were not significant compared to the results for offshore earthquakes along the Nankai Trough (Figure 8 of Takemura et al. 2020).

On the other hand, we found that the *Mw* values based on the 3D CMT analyses were systematically smaller than those in the F-net MT catalog (Figure 4c). The *Mw* values are very important for ground motion simulations because seismic moments are directly related to the amplitude of the ground motion. We also evaluated the differences in *Mw* between 3D CMT and F-net MT solutions along the Nankai Trough using the results from (Takemura et al. 2020; https://doi.org/10.5281/zenodo.3674161). We found both larger and smaller *Mw* values, compared to the F-net catalog, in the Nankai region (Figure 5). In the Kanto and Nankai regions, the differences in *Mw* for offshore earthquakes were larger than those of onshore earthquakes, which may be caused by 3D heterogeneities.

To investigate the cause of these *Mw* differences, we conducted ground motion simulations for the *Mw* 4.36 earthquake of 10:02:45 (JST) November 17, 2017 (Event a) and the *Mw* 4.35 earthquake of 19:56:05 (JST) on August 6, 2018 (Event b). Using the 3D CMT method, Events a and b were located just below the upper surface of the oceanic crust layer 2 and at the boundary between oceanic crust layers 2 and 3 of the Pacific Plate, respectively. The *Mw* differences for Events a and b were -0.31 and -0.25, respectively, and the estimated seismic moments of the 3D CMT solutions were approximately 35% and 42% of the F-net 1D solutions, respectively. We conducted simulations using the same source models and three different heterogeneous models: the JIVSM (Koketsu et al. 2012), JIVSM without sediments, and F-net 1D model (Kubo et al. 2002). The source models were the optimal 3D CMT solutions of the two earthquakes (Events a and b in Table 3).

Figure 6 compares the simulated and observed vertical velocity seismograms at two of the F-net stations; other simulation results are available at https://doi.org/10.5281/zenodo.3926888. We found that simulation results, using the JIVSM and JIVSM without sediments, reproduced observed F-net seismograms, with the single exception of the N.JIZF seismograms for the JIVSM without sediments. This suggests that the effects of low-velocity sediments, around the Kanto region, on CMT inversion using long-period (25–100 s) seismograms are minor. On the other hand, in the Nankai region, a thick low-velocity accretionary prism has a significant influence on seismograms even for periods of 25–100 s. This difference could be explained by the differences in sediment thicknesses in the Kanto Basin (~ 3 km) and the Nankai accretionary prism (~ 5 km). Because the Kanto Basin and its marine sediments exist along the path from Event b to N.JIZF, the differences in the waveforms at N.JIZF, for the periods of 10–50 s, might occur. Around the Nankai Trough, the thicker accretionary prism has a significant influence on surface waves even for periods longer than 20 s, and consequently affects the results from CMT inversions and ground motion simulations (e.g., Nakamura et al. 2015; Takemura et al. 2018b, a, 2019a, b, 2020).

On the other hand, the amplitudes of simulation seismograms, with a similar source and using the F-net 1D model, were approximately 35–45% of observed amplitudes. The effects of the Kanto Basin had minor influence on ground motion at outcrop rock sites (F-net); however, the differences in mechanisms and depths, compared with F-net solutions, were not significant. This could be explained by the differences in heterogeneities around the seismic source. The 3D CMT solutions of Events a and b were located just beneath the upper surface of the oceanic crust layer 2 and near the boundary between oceanic crust layers 2 and 3 of the Pacific Plate, respectively. In the JIVSM (Table 1), the rigidities of the source areas for the two events were in the range 20.4–34.3 GPa. In contrast, the rigidity at depths between 33 and 100 km was a uniform value (63.7 GPa; Table 2) in the F-net 1D model. The differences in rigidities around source regions between the JIVSM and the F-net 1D model correspond to the differences in seismic moments between the 3D CMT and F-net MT solutions (34–42%).

We also simulated long-period ground motions for CMT solutions with *Mw* differences equal to or smaller than -0.2. The simulated earthquakes are listed in Table S1. Amplitude differences at each station were calculated by dividing the maximum simulated amplitudes in the F-net 1D model by those in the JIVSM. Maximum amplitudes were measured using vertical seismograms for the periods of 25–100 s. At almost all stations, amplitudes using the JIVSM were larger than those using the F-net 1D model (Figure 7). Due to structural differences and radiation pattern of the assumed sources, the relationship between Mw and amplitude differences did not exhibit a simple linear trend; however, amplitude differences tended to increase with decreasing Mw difference (-0.2 to -0.3). As such, it may be concluded that the major cause of the differences in seismic moments between the 3D CMT and F-net 1D MT solutions is the difference in modeled rigidity around the source areas.

For the Nankai Trough, both the overestimations and underestimations of seismic moments compared to the F-net catalog were observed (Figure 5). Large *Mw* differences only appeared in the offshore region, where many intraslab and interplate earthquakes occurred. In particular, intraslab earthquakes along the Nankai Trough occurred within the low-velocity oceanic crust and high-velocity oceanic mantle (see Figures 5 and 6 of Takemura et al. 2020), which were not modeled in the F-net 1D model. The difference in *Mw* values along the Nankai Trough could also be explained by the differences in heterogeneous structures in the 3D and 1D models.

In the F-net system, origin times and epicenters were fixed at values in the Japan Meteorological Agency unified hypocenter catalog, and time shifts between observed and synthetic seismograms at each station were enabled. Miyoshi et al. (2017) noticed that prior to estimating structural properties, the reevaluation of centroid times for F-net MT solutions is required to obtain suitable waveform inversion results. In this study, we found that the estimation of seismic moments was affected by the rigidity structure around the source region. The differences in the estimation of seismic moments directly impact the amplitude of ground motion simulations. The amplitude of ground motion simulation is important for evaluating seismic hazards and estimating structural properties along propagation paths. For the 3D forward and inverse modeling of seismic ground motion, a 3D CMT solution should be used for observed and synthetic seismograms in the assumed local 3D model.

Long-period ground motion simulations in the Kanto region

Using our 3D CMT analysis, based on the JIVSM, we simulated long-period ground motions and compared them with the observed seismograms. Due to the SNR of the MeSO-net for periods longer than 5 s, three earthquakes, with an *Mw* equal to or larger than 5.5, were selected for the simulations of long-period ground motion in the Kanto Basin. The source parameters of the selected Events (A–C) are listed in Table 3. Complete files of simulated velocity waveforms and wavefields are available online at https://doi.org/10.5281/zenodo.3926888.

Figure 8 shows an example of the simulated vertical velocity wavefields for the Event A at 40, 60, 80, 100, 120, 140, 160, and 180 s from the earthquake origin (a movie file is also available from https://doi.org/10.5281/zenodo.3926888). The seismic waves radiated from the source complicatedly propagate through the Kanto region. In the Kanto, Niigata, and other offshore regions, the wavelengths and propagation speeds of the Rayleigh waves became shorter and slower because of low-velocity sediments. The energy of these shorter-wavelength components (i.e., long-period ground motion) is trapped within low-velocity sediments. Thus, the duration of long-period ground motion tends to be elongated in the Kanto, Niigata, and offshore regions (lapse time of 180 s). Peak ground velocities (PGVs) were calculated as the vector sum of three-component filtered seismograms at the F-net and MeSO-net stations; the passband period was 5–30 s. Figure 9 shows the spatial distributions of PGVs for each event. Except for Event C, the simulations were able to roughly reproduce the observed PGV features. Large PGVs appeared in regions with bedrock depths greater than 3 km.

Figures 10, 11, and 12 compare the observed and simulated filtered seismograms (15–30 s, 10–20 s, and 5–16 s). We selected two F-net stations and three MeSO-net stations. The selected MeSO-net stations are located at the site with deeper (> 3 km) bedrock depths. The simulations reproduced the observed seismograms at two F-net stations (N.ASIF and N.JIZF), with the exception of the simulation results for Event C for the periods of 5–16 s. These results suggest that these 3D CMT solutions have the ability to reproduce observed ground motion with sufficient accuracy for periods longer than 5 s at F-net stations at outcrop rock sites. Although the seismograms observed at the MeSO-net stations were reproduced by the simulated seismograms for periods longer than 10 s, with the exception of the later phases at E.YROM, the simulation results for 5–16 s periods did not reproduce the observed seismograms in the Kanto Basin. This period band includes the dominant period (~6 s) of long-period ground motions within the Kanto Basin (e.g., Yoshimoto and Takemura 2014). These seismogram discrepancies at the MeSO-net stations could be produced by the JIVSM sedimentary structure. For Event C, because the centroid depth was 8 km, the ground motions for 10–20 s and 5–16 s periods were affected by the Kanto Basin and oceanic sediments from the epicenter to coastal regions. Thus, these sedimentary structures in the offshore region may have decreased the waveform fitness for this event. The overestimation of PGVs (Figure 9c) may also be attributed to the models of the Kanto Basin and the oceanic sediments along propagation paths.

We also conducted the simulations of long-period ground motions using F-net MT solutions. The correlation coefficients of *P*-wave radiation patterns for Events A–C were 0.99, 0.91, and 0.91, respectively, and the depth differences from the F-net solutions are 9, -2, and -6 km, respectively. Simulations from the F-net solutions (Figures S5-7) could not reproduce the observed seismograms, and discrepancies from observations could not be corrected by simple adjustment of seismic moments. This implies that although the differences in the focal mechanisms and depths estimated by our 3D and F-net 1D catalogs were not so significant, our solutions improve the reproducibility of broadband (5–100 s) seismograms at stations with/without the Kanto Basin.

Conclusions

We conducted CMT inversions of moderate earthquakes in the Kanto region from April 2017 to March 2020. The estimated focal mechanisms and depths using the 3D CMT method were not significantly different from the corresponding F-net MT solutions. However, the *Mw* values were systematically smaller than those in the F-net catalog. Earthquakes with large *Mw* differences tended to be located within the subducting plate, i.e., intraslab earthquakes. Using numerical simulations with 3D and 1D velocity models, we concluded that the major cause for the *Mw* differences is the difference in rigidity between the 1D and 3D velocity models. The 3D subducting oceanic crust and mantle could not be modeled in the 1D CMT system. The differences in the estimation of seismic moments directly affect the amplitude of ground motion simulations. The 3D simulation of an intraslab earthquake using the 1D CMT catalog can cause amplitude overestimation, even at outcrop rock sites. 3D CMT solutions should be adopted for precise forward and inverse modeling of long-period ground motions.

In this study, simulations using 3D CMT solutions and the JIVSM were able to reproduce ground motion for periods longer than 5 s at outcrop rock sites. On the other hand, discrepancies between observations and simulations using F-net solutions could not be corrected by simple adjustment of seismic moments. These results indicate that the 3D CMT inversion works well in the Kanto region, and 3D CMT solutions are suitable for modeling long-period (> 5 s) ground motion. However, while simulations at stations within the Kanto Basin effectively reproduced observed seismograms for periods longer than 10 s, the reproducibility of these simulations decreased for periods shorter than 10 s.

In the Kanto region because the predominant period of long-period ground motion is approximately 6 s, a well-constrained sedimentary model is required to evaluate long-period ground motion for observed and anticipated large earthquakes. Recently, other regional/local velocity structure models of the sedimentary basin and subducting oceanic plate have been released (e.g., Hirose et al. 2008; Takemura et al. 2015; Headquarters for Earthquake Research Promotion 2017; Ito et al. 2019). The reproducibility of long-period ground motion in the Kanto Basin can potentially be improved through the utilization of other published or adjusted models based on ground motion simulations; this should be the primary focus of future research.

Abbreviations

1D

one-dimensional

3D

three-dimensional

CMT

centroid moment tensor

ERI-JURP

Earthquake Research Institute, the University of Tokyo Joint Usage/Research Program

F-net

Full-range seismograph network

JIVSM

Japan Integrated Velocity Structure Model version 1

JST

Japan Standard Time

MeSO-net

Metropolitan Seismic Observation network

MT
moment tensor
NIED
National Research Institute for Earth Science and Disaster Resilience
OpenSWPC
Open-Source Seismic Wave Propagation Code
SAC
Seismic Analysis Code
SNR
Signal to noise
UTC
Coordinated Universal Time
VR
Variance Reduction

Declarations

Ethics approval and consent to participate

Not applicable.

Consent for publication

Not applicable.

Competing interests

The authors declare that they have no competing interests.

Availability of data and materials

Using HinetPy (https://doi.org/10.5281/zenodo.3695076), NIED F-net and MeSO-net data were downloaded from https://hinetwww11.bosai.go.jp/auth/?LANG=en. We used the open-source code OpenSWPC version 5.0.2 (https://doi.org/10.5281/zenodo.3712650) and the local 3D model "JIVSM" by Koketsu et al. (2012) from https://www.jishin.go.jp/evaluation/seismic_hazard_map/lpshm/12_choshuki_dat/. Figure images were drawn using Generic Mapping Tools (Wessel et al. 2013) and the Seismic Analysis Code (Goldstein and Snoke 2005; Helffrich et al. 2013) was used in some signal processing works. The CMT solutions in Takemura et al. (2020) and this study are available from https://doi.org/10.5281/zenodo.3674161 and https://doi.org/10.5281/zenodo.3926884, respectively. Simulation results for long-period ground motion are also available at https://doi.org/10.5281/zenodo.3926888.

Funding

This study was supported by the JSPS KAKENHI grant number 19H04626 in Scientific Research on Innovative Areas “Science of slow earthquakes” This study was also supported by the ERI JURP 2020-S-04.

Authors' contributions

ST conducted a numerical simulation to synthesize Green’s functions and long-period ground motion, CMT inversions of moderate size earthquakes in the Kanto region, and drafted the manuscript. ST and KY investigated propagation features of long-period ground motions. ST and KS interpreted the local seismicity beneath Kanto region. All authors have read and approved the final manuscript.

Acknowledgements

Numerical simulations of seismic wave propagation were conducted using the computer system of the Earthquake and Volcano Information Center at the Earthquake Research Institute, the University of Tokyo, and Fujitsu PRIMERGY CX600M1/CX1640M1 (Oakforest-PAC) at the Information Technology Center, the University of Tokyo. We thank Ryo Okuwaki for useful discussions. We would like to thank Editage (www.editage.com) for English language editing. We also thank Dr B. Hejrani, an anonymous reviewer and Editor Prof. K. Yoshizawa for careful reviewing and constructive comments, which have helped to improve the manuscript.

Authors' information

Shunsuke TAKEMURA, http://orcid.org/0000-0002-7511-3443 Earthquake Research Institute, the University of Tokyo, 1-1-1 Yayoi, Bunkyo-ku, Tokyo, 113-0032, Japan, shunsuke@eri.u-tokyo.ac.jp

Kazuo YOSHIMOTO, https://orcid.org/0000-0003-2411-948X Graduate School of Nanobioscience, Department of Material System Science, Yokohama City University, 22-2 Seto, Kanazawa-ku, Yokohama 236-0027, Japan, k_yoshi@yokohama-cu.ac.jp

Katsuhiko SHIOMI, https://orcid.org/0000-0003-3566-0749 Earthquake and Tsunami Research Division, National Research Institute for Earth Science and Disaster Resilience, 3-1 Tennodai, Tsukuba, Ibaraki 305-0006, Japan, shiomi@bosai.go.jp

References

Agata R (2020) Introduction of covariance components in slip inversion of geodetic data following a non-uniform spatial distribution and application to slip deficit rate estimation in the Nankai Trough subduction zone. Geophys J Int 221:1832–1844. https://doi.org/10.1093/gji/ggaa116

Baba S, Takemura S, Obara K, Noda A (2020) Slow earthquakes illuminating interplate coupling heterogeneities in subduction zones. Geophys Res Lett. https://doi.org/10.1029/2020GL088089

Bernardi F, Braunmiller J, Kradolfer U, Giardini D (2004) Automatic regional moment tensor inversion in the European-Mediterranean region. Geophys J Int 157:703–716. https://doi.org/10.1111/j.1365-246X.2004.02215.x

Boore DM (1999) Basin Waves on a Seafloor Recording of the 1990 Upland, California, Earthquake: Implications for Ground Motions from a Larger Earthquake. Bull Seismol Soc Am 89:317–324

Day SM, Graves R, Bielak J, et al (2008) Model for Basin Effects on Long-Period Response Spectra in Southern California. Earthq Spectra 24:257–277. https://doi.org/10.1193/1.2857545

Ekström G, Nettles M, Dziewoński AM (2012) The global CMT project 2004-2010: Centroid-moment tensors for 13,017 earthquakes. Phys Earth Planet Inter 200–201:1–9. https://doi.org/10.1016/j.pepi.2012.04.002

Fukuyama E, Ishida M, Dreger DS, Kawai H (1998) Automated seismic moment tensor determination by using on-line broadband seismic waveforms. Zisin 51:149–156. https://doi.org/10.4294/zisin1948.51.1_149

Furumura M, Furumura T, Wen KL (2001) Numerical simulation of Love wave generation in the Ilan Basin, Taiwan, during the 1999 Chi-Chi earthquake. Geophys Res Lett 28:3385–3388. https://doi.org/10.1029/2001GL013114

Furumura T, Hayakawa T (2007) Anomalous propagation of long-period ground motions recorded in Tokyo during the 23 October 2004 Mw 6.6 Niigata-ken Chuetsu, Japan, earthquake. Bull Seismol Soc Am 97:863–880. https://doi.org/10.1785/0120060166

Furumura T, Hayakawa T, Nakamura M, et al (2008) Development of long-period ground motions from the Nankai trough, Japan, earthquakes: Observations and computer simulation of the 1944 Tonankai (Mw 8.1) and the 2004 SE Off-Kii Peninsula (Mw 7.4) earthquakes. Pure Appl Geophys 165:585–607. https://doi.org/10.1007/s00024-008-0318-8

Gao H, Shen Y (2014) Upper mantle structure of the Cascades from full-wave ambient noise tomography: Evidence for 3D mantle upwelling in the back-arc. Earth Planet Sci Lett 390:222–233. https://doi.org/10.1016/j.epsl.2014.01.012

Gokhberg A, Fichtner A (2016) Full-waveform inversion on heterogeneous HPC systems. Comput Geosci 89:260–268. https://doi.org/10.1016/j.cageo.2015.12.013

Goldstein P, Snoke A (2005) SAC Availability for the IRIS Community. In: Inc. Institutions Seismol. Data Manag. Cent. Electron. Newsl. https://ds.iris.edu/ds/newsletter/vol7/no1/193/sac-availability-for-the-iris-community/

Gomberg J (2018) Cascadia Onshore-Offshore Site Response, Submarine Sediment Mobilization, and Earthquake Recurrence. J Geophys Res Solid Earth 123:1381–1404.

https://doi.org/10.1002/2017JB014985

Guo Y, Koketsu K, Miyake H (2016) Propagation mechanism of long-period ground motions for offshore earthquakes along the nankai trough: Effects of the accretionary wedge. Bull Seismol Soc Am 106:1176–1197. https://doi.org/10.1785/0120150315

Headquarters for Earthquake Research Promotion (2017) National seismic hazard maps for Japan. https://www.jishin.go.jp/evaluation/seismic_hazard_map/shm_report/shm_report_2017/

Hejrani B, Tkalčić H (2020) Resolvability of the centroid-moment-tensors for shallow seismic sources and improvements from modelling high-frequency waveforms. J Geophys Res Solid Earth. https://doi.org/10.1029/2020JB019643

Hejrani B, Tkalčić H, Fichtner A (2017) Centroid moment tensor catalogue using a 3-D continental scale Earth model: Application to earthquakes in Papua New Guinea and the Solomon Islands. J Geophys Res Solid Earth 122:5517–5543. https://doi.org/10.1002/2017JB014230

Helffrich G, Wookey J, Bastow I (2013) The Seismic Analysis Code. Cambridge University Press, Cambridge

Helffrich GR (1997) How good are routinely determined focal mechanisms? Empirical statistics based on a comparison of Harvard, USGS and ERI moment tensors. Geophys J Int 131:741–750. https://doi.org/10.1111/j.1365-246X.1997.tb06609.x

Hirose F, Nakajima J, Hasegawa A (2008) Three-dimensional seismic velocity structure and configuration of the Philippine Sea slab in southwestern Japan estimated by double-difference tomography. J Geophys Res Solid Earth 113:1–26. https://doi.org/10.1029/2007JB005274

Ito A, Sugioka H, Obana K, et al (2017a) Upper boundaries of the Pacific and Philippine Sea plates near the triple junction off the Boso Peninsula deduced from ocean-bottom seismic observations. Earth, Planets Sp 69:30. https://doi.org/10.1186/s40623-017-0608-4

Ito A, Tonegawa T, Uchida N, et al (2019) Configuration and structure of the Philippine Sea Plate off Boso, Japan: constraints on the shallow subduction kinematics, seismicity, and slow slip events. Earth, Planets Sp 71:111. https://doi.org/10.1186/s40623-019-1090-y

Ito A, Yamamoto Y, Hino R, et al (2017b) Tomographic image of crust and upper mantle off the Boso Peninsula using data from an ocean - bottom seismograph array. Earth, Planets Sp. https://doi.org/10.1186/s40623-017-0703-6

Iwaki A, Maeda T, Morikawa N, et al (2018) Effects of random 3D upper crustal heterogeneity on long-period (≥ 1 s) ground-motion simulations. Earth, Planets Sp 70:156. https://doi.org/10.1186/s40623-018-0930-5

Kanamori H, Brodsky EE (2004) The physics of earthquakes. Reports Prog Phys 67:1429–1496. https://doi.org/10.1088/0034-4885/67/8/R03

Kaneko Y, Ito Y, Chow B, et al (2019) Ultra-long Duration of Seismic Ground Motion Arising From a Thick, Low-Velocity Sedimentary Wedge. J Geophys Res Solid Earth 124:10347–10359. https://doi.org/10.1029/2019JB017795

Kasahara K, Morita Y, Hirata N, et al (2009) Development of the Metropolitan Seismic Observation network (MeSO-net) for Detection of Mega-thrust beneath Tokyo Metropolitan Area. Bull Earthq Res Inst Univ Tokyo 2:71–88

Kennett BLN, Fichtner A, Fishwick S, Yoshizawa K (2013) Australian seismological referencemodel (AuSREM): Mantle component. Geophys J Int 192:871–887. https://doi.org/10.1093/gji/ggs065

Kimura T, Murakami H, Matsumoto T (2015) Systematic monitoring of instrumentation health in high-density broadband seismic networks. Earth, Planets Sp 67:55. https://doi.org/10.1186/s40623-015-0226-y

Kinoshita S, Fujiwara H, Mikoshiba T, Hoshino T (1992) Secondary Love waves observed by a strong-motion array in the Tokyo lowlands, Japan. J Phys Earth 40:99–116. https://doi.org/10.4294/jpe1952.40.99

Koketsu K, Kikuchi M (2000) Propagation of seismic ground motion in the Kanto basin, Japan. Science (80-) 288:1237–1239. https://doi.org/10.1126/science.288.5469.1237

Koketsu K, Miyake H (2008) A seismological overview of long-period ground motion. J Seismol 12:133–143. https://doi.org/10.1007/s10950-007-9080-0

Koketsu K, Miyake H, Afnimar, Tanaka Y (2009) A proposal for a standard procedure of modeling 3-D velocity structures and its application to the Tokyo metropolitan area, Japan. Tectonophysics 472:290–300. https://doi.org/10.1016/j.tecto.2008.05.037

Koketsu K, Miyake H, Suzuki H (2012) Japan Integrated Velocity Structure Model Version 1. Proc 15th World Conf Earthq Eng 1–4

Komatitsch D (2004) Simulations of Ground Motion in the Los Angeles Basin Based upon the Spectral-Element Method. Bull Seismol Soc Am 94:187–206. https://doi.org/10.1785/0120030077

Kubo A, Fukuyama E, Kawai H, Nonomura K (2002) NIED seismic moment tensor catalogue for regional earthquakes around Japan: Quality test and application. Tectonophysics 356:23–48. https://doi.org/10.1016/S0040-1951(02)00375-X

Kuge K, Kawakatsu H (1993) Significance of non-double couple components of deep and intermediate-depth earthquakes: implications from moment tensor inversions of long-period seismic waves. Phys

Earth Planet Inter 75:243–266. https://doi.org/10.1016/0031-9201(93)90004-S

Lee S-J, Liang WT, Cheng HW, et al (2013) Towards real-time regional earthquake simulation I: Real-time moment tensor monitoring (RMT) for regional events in Taiwan. Geophys J Int 196:432–446. https://doi.org/10.1093/gji/ggt371

Maeda T, Takemura S, Furumura T (2017) OpenSWPC: an open-source integrated parallel simulation code for modeling seismic wave propagation in 3D heterogeneous viscoelastic media. Earth, Planets Sp 69:102. https://doi.org/10.1186/s40623-017-0687-2

Matsubara M, Obara K (2011) The 2011 off the Pacific coast of Tohoku Earthquake related to a strong velocity gradient with the Pacific plate. Earth, Planets Sp 63:663–667. https://doi.org/10.5047/eps.2011.05.018

Matsubara M, Obara K, Kasahara K (2008) Three-dimensional P- and S-wave velocity structures beneath the Japan Islands obtained by high-density seismic stations by seismic tomography. Tectonophysics 454:86–103. https://doi.org/10.1016/j.tecto.2008.04.016

Miyake H, Koketsu K (2005) Long-period ground motions from a large offshore earthquake: The case of the 2004 off the Kii peninsula earthquake, Japan. Earth, Planets Sp 57:203–207. https://doi.org/10.1186/BF03351816

Miyazawa M (2016) An investigation into the remote triggering of the Oita earthquake by the 2016 Mw 7.0 Kumamoto earthquake using full wavefield simulation. Earth, Planets Sp 68:. https://doi.org/10.1186/s40623-016-0585-z

Miyoshi T, Obayashi M, Peter D, et al (2017) Adjoint tomography of the crust and upper mantle structure beneath the Kanto region using broadband seismograms. Prog Earth Planet Sci 4:29. https://doi.org/10.1186/s40645-017-0143-8

Mukai Y, Furumura T, Maeda T (2018) Causes of Azimuthally Dependent Amplification Variations of Long-period Ground Motions in the Kanto Basin , Central Japan. Bull Earthq Res Inst Univ Tokyo 93:31–48

Nakamura T, Takenaka H, Okamoto T, et al (2015) Long-period ocean-bottom motions in the source areas of large subduction earthquakes. Sci Rep 5:1–2. https://doi.org/10.1038/srep16648

National Research Institute for Earth Science and Disaster Resilience (2019) NIED F-net. In: Natl. Res. Inst. Earth Sci. Disaster Resil. https://doi.org/10.17598/NIED.0005

Oba A, Furumura T, Maeda T (2020) Data Assimilation-Based Early Forecasting of Long-Period Ground Motions for Large Earthquakes Along the Nankai Trough. J Geophys Res Solid Earth 125:. https://doi.org/10.1029/2019JB019047

Okada Y, Kasahara K, Hori S, et al (2004) Recent progress of seismic observation networks in Japan —Hi-net, F-net, K-NET and KiK-net—. Earth, Planets Sp 56:xv–xxviii. https://doi.org/10.1186/BF03353076

Okamoto T, Takenaka H, Nakamura T (2018) Evaluation of accuracy of synthetic waveforms for subduction-zone earthquakes by using a land–ocean unified 3D structure model. Earth, Planets Sp 70:. https://doi.org/10.1186/s40623-018-0871-z

Olsen KB, Day SM, Minster JB, et al (2006) Strong shaking in Los Angeles expected from southern San Andreas earthquake. Geophys Res Lett 33:L07305. https://doi.org/10.1029/2005GL025472

Ryoki K (1999) Three-Dimensional Depth Structure of the Crust and Uppermost Mantle beneath Southwestern Japan and Its Regional Gravity Anomalies. Zisin (Journal Seismol Soc Japan 2nd ser) 52:51–63. https://doi.org/10.4294/zisin1948.52.1_51

Sakai S, Hirata N (2009) Distribution of the Metropolitan Seismic Observation network. Bull Earthq Res Inst Tokyo Univ 84:57–69

Stephenson WJ, Reitman NG, Angster SJ (2017) P- and S-wave velocity models incorporating the Cascadia subduction zone for 3D earthquake ground motion simulations, Version 1.6—Update for Open-File Report 2007–1348

Takemura S, Akatsu M, Masuda K, et al (2015) Long-period ground motions in a laterally inhomogeneous large sedimentary basin: observations and model simulations of long-period surface waves in the northern Kanto Basin, Japan. Earth, Planets Sp 67:33. https://doi.org/10.1186/s40623-015-0201-7

Takemura S, Kimura T, Saito T, et al (2018a) Moment tensor inversion of the 2016 southeast offshore Mie earthquake in the Tonankai region using a three-dimensional velocity structure model: effects of the accretionary prism and subducting oceanic plate. Earth, Planets Sp 70:50. https://doi.org/10.1186/s40623-018-0819-3

Takemura S, Kubo H, Tonegawa T, et al (2019a) Modeling of Long-Period Ground Motions in the Nankai Subduction Zone: Model Simulation Using the Accretionary Prism Derived from Oceanfloor Local S-Wave Velocity Structures. Pure Appl Geophys 176:627–647. https://doi.org/10.1007/s00024-018-2013-8

Takemura S, Matsuzawa T, Kimura T, et al (2018b) Centroid Moment Tensor Inversion of Shallow Very Low Frequency Earthquakes Off the Kii Peninsula, Japan, Using a Three-Dimensional Velocity Structure Model. Geophys Res Lett 45:6450–6458. https://doi.org/10.1029/2018GL078455

Takemura S, Matsuzawa T, Noda A, et al (2019b) Structural Characteristics of the Nankai Trough Shallow Plate Boundary Inferred From Shallow Very Low Frequency Earthquakes. Geophys Res Lett 46:4192–4201. https://doi.org/10.1029/2019GL082448

Takemura S, Okuwaki R, Kubota T, et al (2020) Centroid moment tensor inversions of offshore earthquakes using a three-dimensional velocity structure model: slip distributions on the plate boundary along the Nankai Trough. Geophys J Int 222:1109–1125. https://doi.org/10.1093/gji/ggaa238

Takemura S, Shiomi K, Kimura T, Saito T (2016) Systematic difference between first-motion and waveform-inversion solutions for shallow offshore earthquakes due to a low-angle dipping slab. Earth, Planets Sp 68:149. https://doi.org/10.1186/s40623-016-0527-9

Takemura S, Shiomi K, Obara K (2019c) 3D simulation of seismic wave propagation during the MJMA 6.3 Hyuga-nada earthquake occurred on 10 May 2019. Rep Coord Comm Earthq Predict Japan 102:320–325

Tape C, Liu Q, Maggi A, Tromp J (2009) Adjoint tomography of the southern california crust. Science (80-) 325:988–992. https://doi.org/10.1126/science.1175298

Vallée M, Charléty J, Ferreira AMG, et al (2011) SCARDEC: A new technique for the rapid determination of seismic moment magnitude, focal mechanism and source time functions for large earthquakes using body-wave deconvolution. Geophys J Int 184:338–358. https://doi.org/10.1111/j.1365-246X.2010.04836.x

Wang X, Zhan Z (2020) Moving from 1-D to 3-D velocity model: automated waveform-based earthquake moment tensor inversion in the Los Angeles region. Geophys J Int 220:218–234. https://doi.org/10.1093/gji/ggz435

Wessel P, Smith WHF, Scharroo R, et al (2013) Generic mapping tools: Improved version released. Eos (Washington DC) 94:409–410. https://doi.org/10.1002/2013EO450001

Wirth EA, Vidale JE, Frankel AD, et al (2019) Source-Dependent Amplification of Earthquake Ground Motions in Deep Sedimentary Basins. Geophys Res Lett 46:6443–6450. https://doi.org/10.1029/2019GL082474

Yoshimoto K, Takemura S (2014) A study on the predominant period of long-period ground motions in the Kanto Basin, Japan. Earth, Planets Sp 66:100. https://doi.org/10.1186/1880-5981-66-100

Tables

Table 1. Physical parameters of each layer in JIVSM. The air and seawater layers were treated as being the same, following Maeda *et al.* (2017). The *P*-wave velocity (V_P), *S*-wave velocity (V_S), density (r), rigidity (m), and inelastic attenuation (Q_P and Q_S) are listed.

	V_P [km/s]	V_S [km/s]	r [kg/m^3]	m [GPa]	Q_P	Q_S
Air	0.0	0.0	0.001	0.0	10^{10}	10^{10}
seawater	1.5	0.0	1.04	0.0	10^6	10^6
Sedimentary layer 1	1.8	0.5	1.95	0.49	170	100
Sedimentary layer 3	2.3	0.9	2.10	1.70	340	200
Sedimentary layer 4	3.0	1.5	2.25	5.06	510	300
Basement	5.5	3.2	2.65	27.1	680	400
Upper crust	5.8	3.4	2.70	31.2	680	400
Lower crust	6.4	3.8	2.80	40.0	680	400
Upper mantle	7.5	4.5	3.20	64.8	850	500
Philippine Sea plate						
Oceanic crust layer 2	5.0	2.9	2.40	20.2	340	200
Oceanic crust layer 3	6.8	4.0	2.90	46.4	510	300
Oceanic Mantle	8.0	4.7	3.20	70.7	850	500
Pacific Plate						
Oceanic crust layer 2	5.4	2.8	2.60	20.4	340	200
Oceanic crust layer 3	6.5	3.5	2.80	34.3	510	300
Oceanic Mantle	8.1	4.6	3.40	71.9	850	500

Table 2. F-net 1D velocity model. The physical parameters are referred from Kubo et al. (2002).

Thickness (Depth) [km]	V_P [km/s]	V_S [km/s]	r [kg/m^3]	m [GPa]	Q_P	Q_S
3 (0–3)	5.5	3.14	2.3	22.7	600	300
15 (3–18)	6.0	3.55	2.4	30.2	600	300
15 (18–33)	6.7	3.83	2.8	41.1	600	300
67 (33–100)	7.8	4.46	3.2	63.7	600	300
125 (100–225)	8.0	4.57	3.3	67.7	600	300
100 (225–325)	8.4	4.80	3.4	78.3	600	300
100 (325–425)	8.6	4.91	3.5	84.4	600	300
–	9.3	5.31	3.7	104	600	300

Table 3. Source parameters of long-period ground motions. Origin times of events a, b, A, B, and C were 10:02:45 JST on November 17, 2017, 19:56:05 JST on August 6, 2018, 19:23:01 JST on August 4, 2019, 03:23:54 JST on January 3, 2020, and 20:19:56 JST on February 6, 2020, respectively. Source durations were assumed using the empirical relationship between seismic moments and durations (Kanamori and Brodsky 2004).

	Lon. [°]	Lat. [°]	Depth [km]	m_{rr}	m_{qq}	m_{ff}	m_{rq}	m_{rf}	m_{fq}	Exp.	Dur. [s]
a	141.4	37.2	44	3.365	-0.118	-1.848	1.191	3.131	-0.649	22	1
b	141.0	35.6	32	2.659	0.623	2.077	-0.707	3.068	-1.249	22	1
A	141.9	37.6	56	2.540	-0.520	-2.144	1.004	2.352	-1.102	25	5
B	141.1	36.0	36	1.128	-0.696	-0.711	0.055	2.408	-0.210	24	3
C	141.8	36.4	8	-1.402	-0.082	0.713	-0.239	1.316	-0.043	24	2

Figures

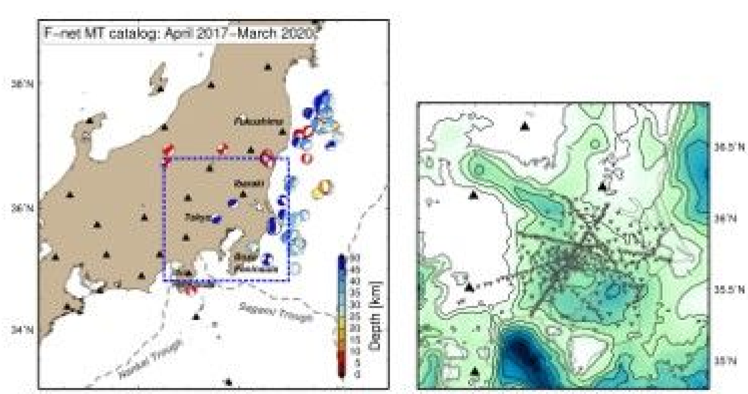

Figure 1

Map of the Kanto region, Japan. The filled black triangles are F-net stations. The plotted focal mechanisms represent moment tensor (MT) solutions listed in the F-net MT catalog. The left panel shows the broader context of the area enclosed by the blue dashed line. Inverse triangles in the left panel are MeSO-net stations. The background contours in the right panel are the bedrock depths of the JIVSM (Koketsu et al. 2012).

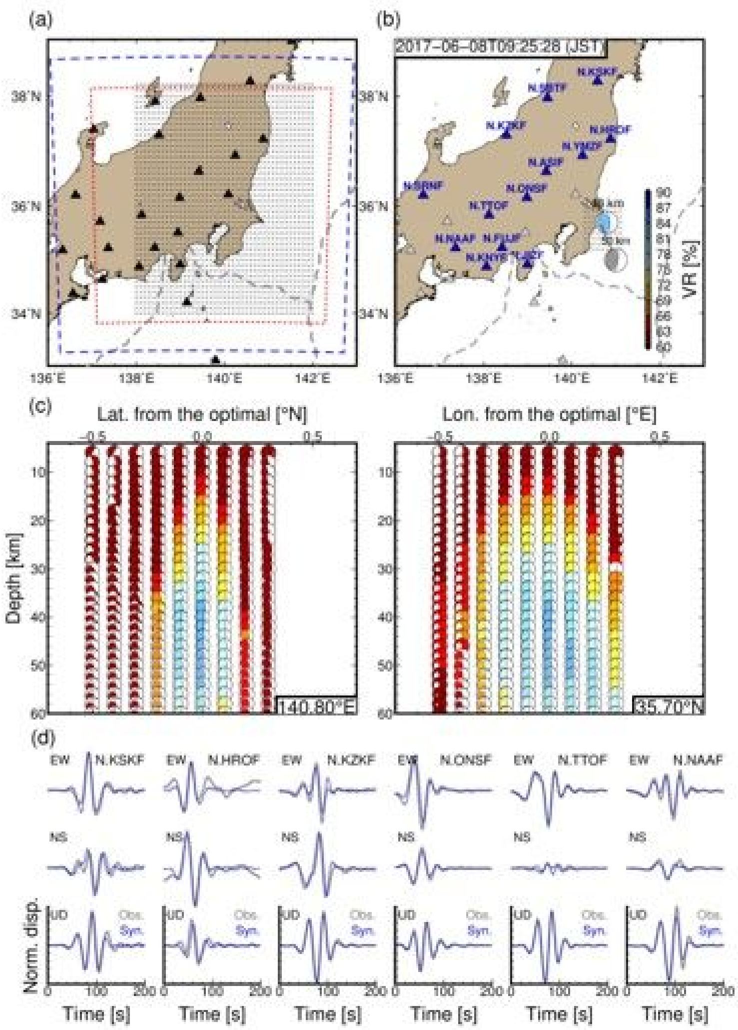

Figure 2

Settings and an example of 3D CMT inversion in the Kanto region. (a) Simulation settings to evaluate Green's functions. The regions enclosed by the blue dashed and red dotted lines represent the horizontal coverage of the simulation model regions for evaluating Green's functions and long-period ground motion simulations, respectively. The triangles denote the locations of the F-net stations and the crosses in the map are the assumed source grids. (b–d) an example of a CMT solution for an earthquake on June 8, 2017, the location and depth of the optimal solution, used stations, and depth variations of optimal solutions at each source grid. Colors of the focal mechanisms reflect variance reduction (VR) between observed and synthetic displacements in the 25–100 s period band. The numbers above the optimal solutions in (b) are the optimal centroid depths. The grey focal mechanism in (b) is the F-net MT solution of this earthquake. The blue triangles in (b) are the used F-net stations. (c) Spatial variations of VRs along latitude-depth and longitude-depth planes. (d) Examples of comparisons between observed and synthetic displacements in the 25–100 s period band. Gray solid and blue dotted lines are the observed and synthetic seismograms, respectively. Synthetic seismograms were evaluated by assuming the optimal solution. Amplitudes at each station were normalized by the maximum amplitude of observed and synthetic three-component displacement waveforms.

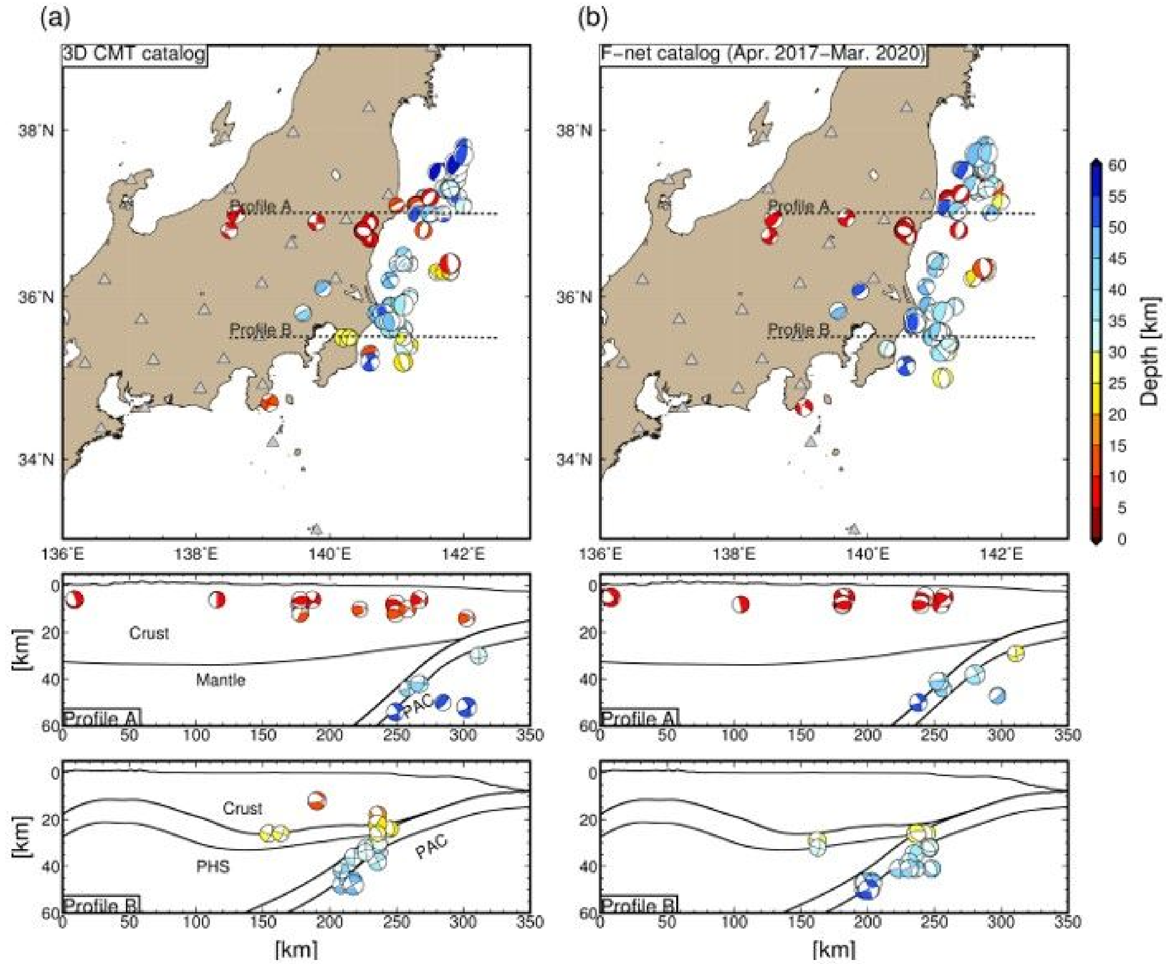

Figure 3

Results of 3D CMT inversion in the Kanto region. (a) 3D CMT catalog (this study), and (b) F-net MT catalog. Upper panels show map views of the focal mechanisms. The colors represent the estimated centroid depth. The bottom panels show cross-sections along profiles A and B. In the bottom panels, topography, Moho, the upper surface of subducting plates, and the oceanic Moho are plotted.

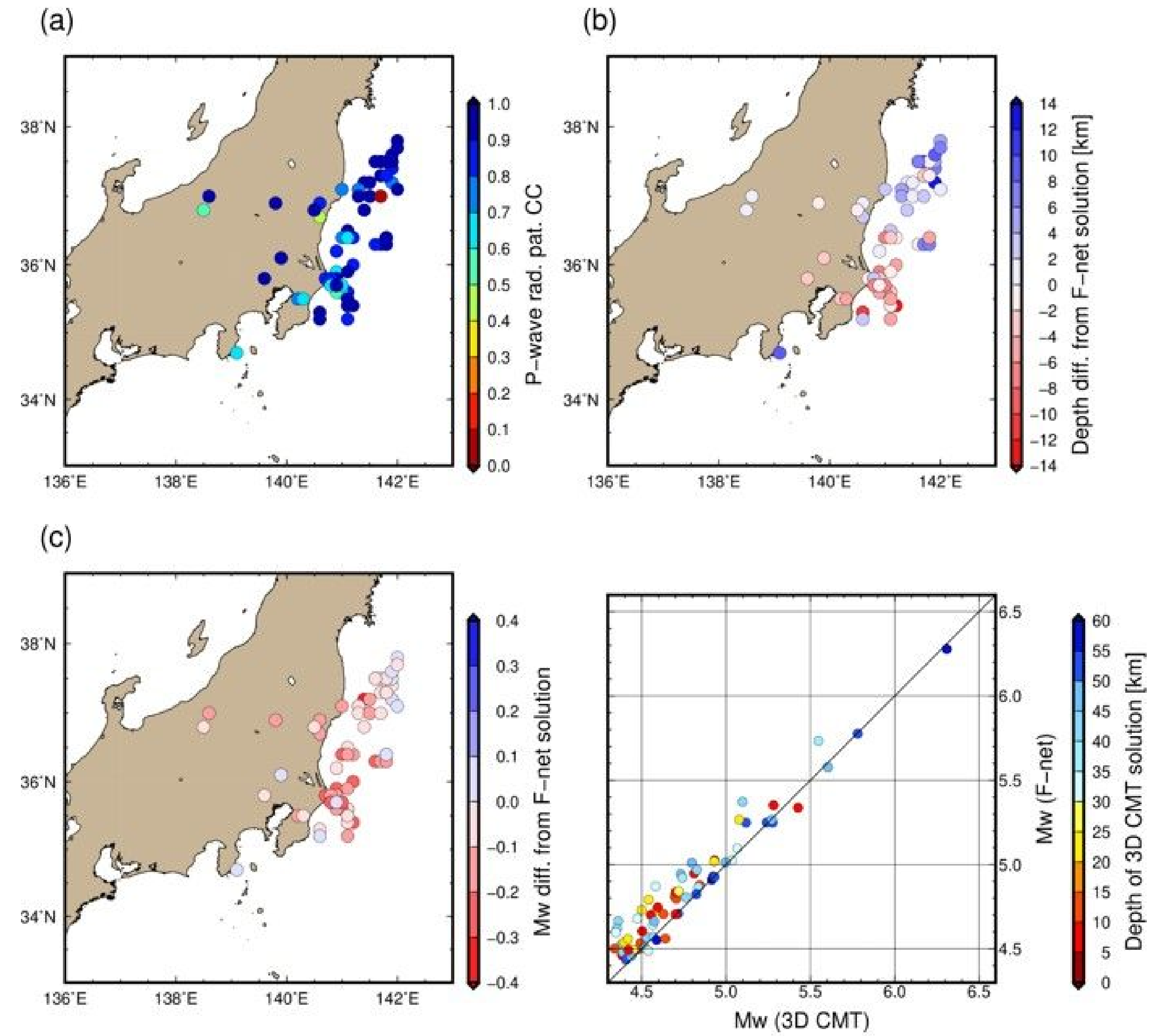

Figure 4

Differences between 3D CMT and F-net MT catalogs in the Kanto region. (a) Cross-correlation of P-wave radiation patterns (e.g., Kuge and Kawakatsu 1993; Helffrich 1997) between 3D CMT and F-net MT catalogs. (b) Depth differences and (c) Mw differences from F-net MT solutions.

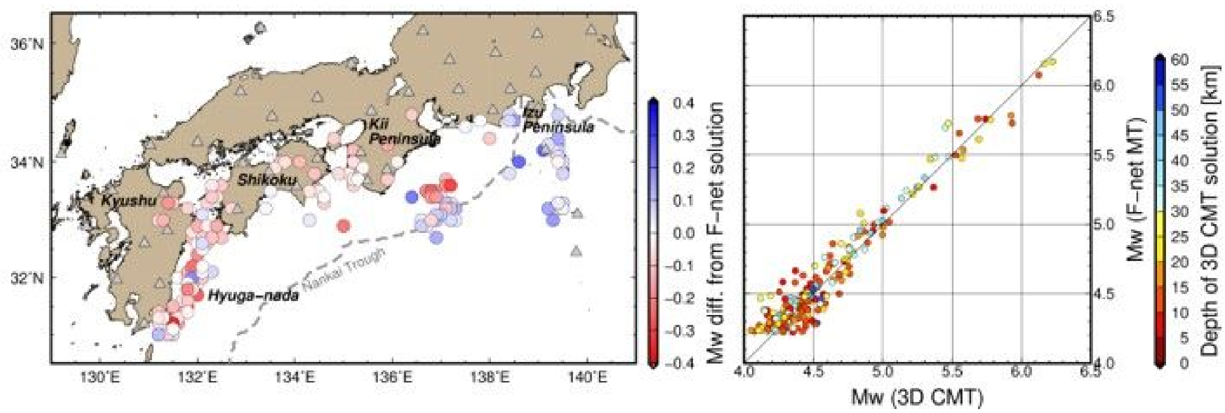

Figure 5

Differences in Mw values between F-net MT and 3D CMT solutions along the Nankai Trough. The 3D CMT catalog along the Nankai Trough is from Takemura et al. (2020).

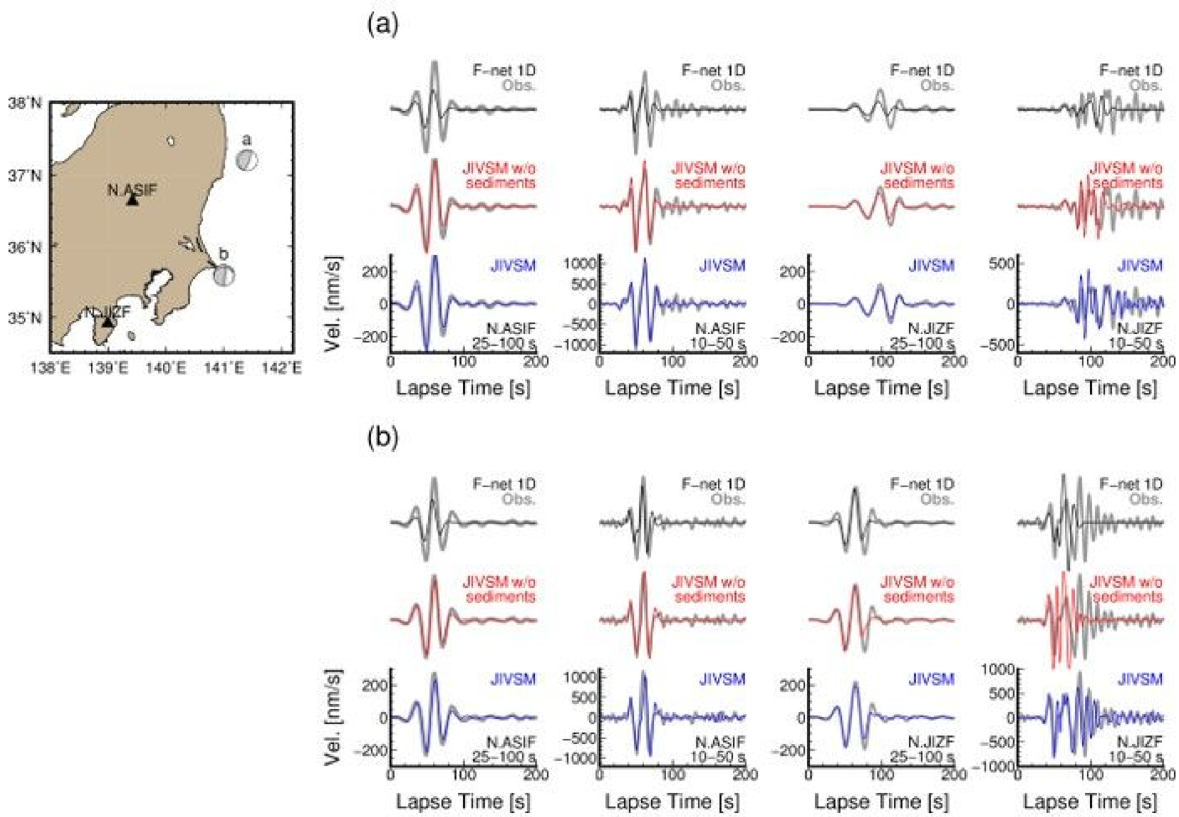

Figure 6

Simulations of long-period ground motion in various models. Simulation results of (a) Event a and (b) Event b. Observed F-net vertical seismograms are represented by bold gray lines. The black, red, and blue lines are simulated vertical seismograms of the JIVSM, JIVSM without sediments, and F-net 1D model, respectively. The physical parameters of sedimentary layers of the JIVSM without sediments were replaced with those of the upper crust (see Table 1). Locations of seismic sources and stations are illustrated in the upper left panel. Plotted focal mechanisms are the optimal solutions of events a and b.

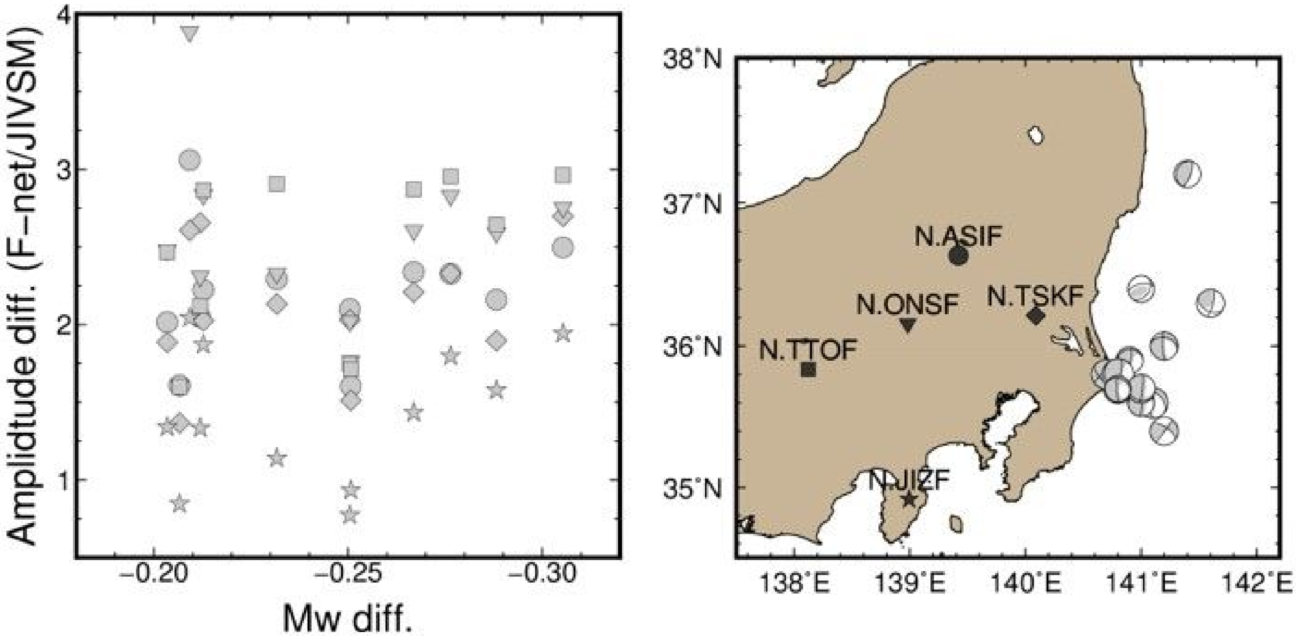

Figure 7

Amplitude differences of simulation results between the JIVSM and F-net 1D model. Circle, diamond, inverse triangle, square, and star represent amplitude ratio or station location of N.ASIF, N.TSKF, N,ONSF, N.TTOF, and N.JIZF, respectively. Amplitudes ratios were calculated by dividing maximum amplitudes of simulations using the F-net 1D model by those using the JIVSM. Maximum amplitudes were measured by using vertical seismograms for the periods of 25–100 s.

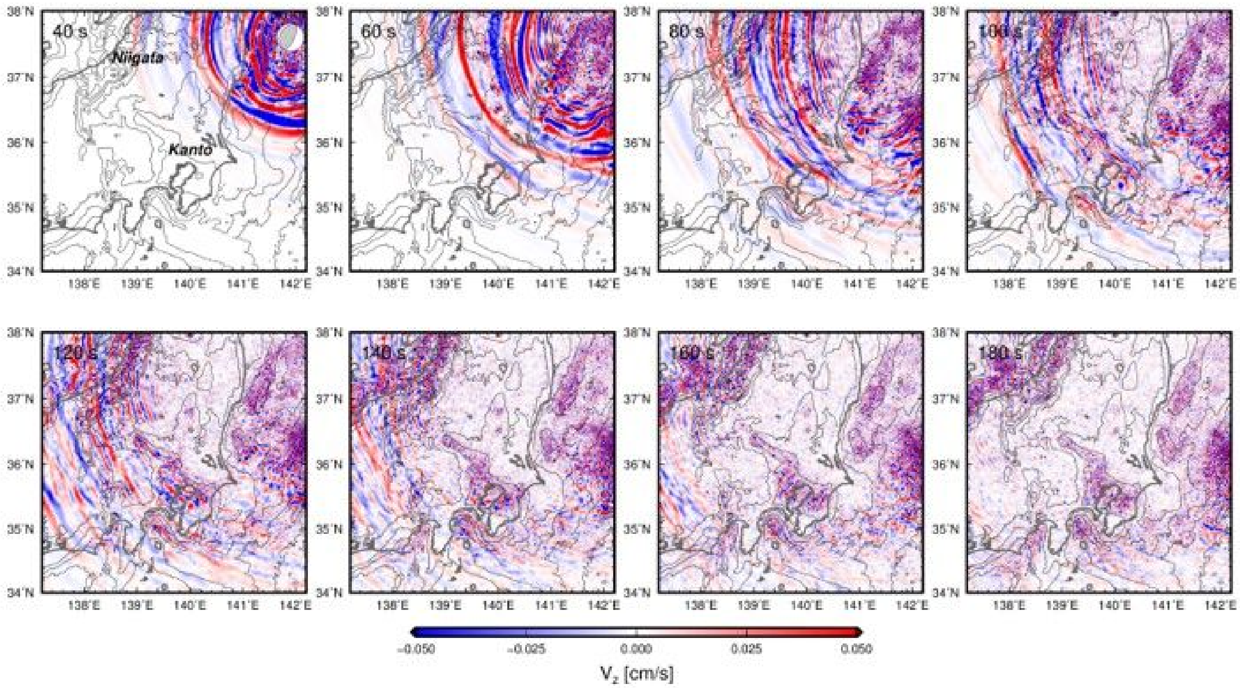

Figure 8

Snapshots of simulated vertical velocity wavefield for Event A. The numbers at the left-top corner are lapse times from the earthquake origin. The contour lines are the JIVSM bedrock depths at 2 km intervals.

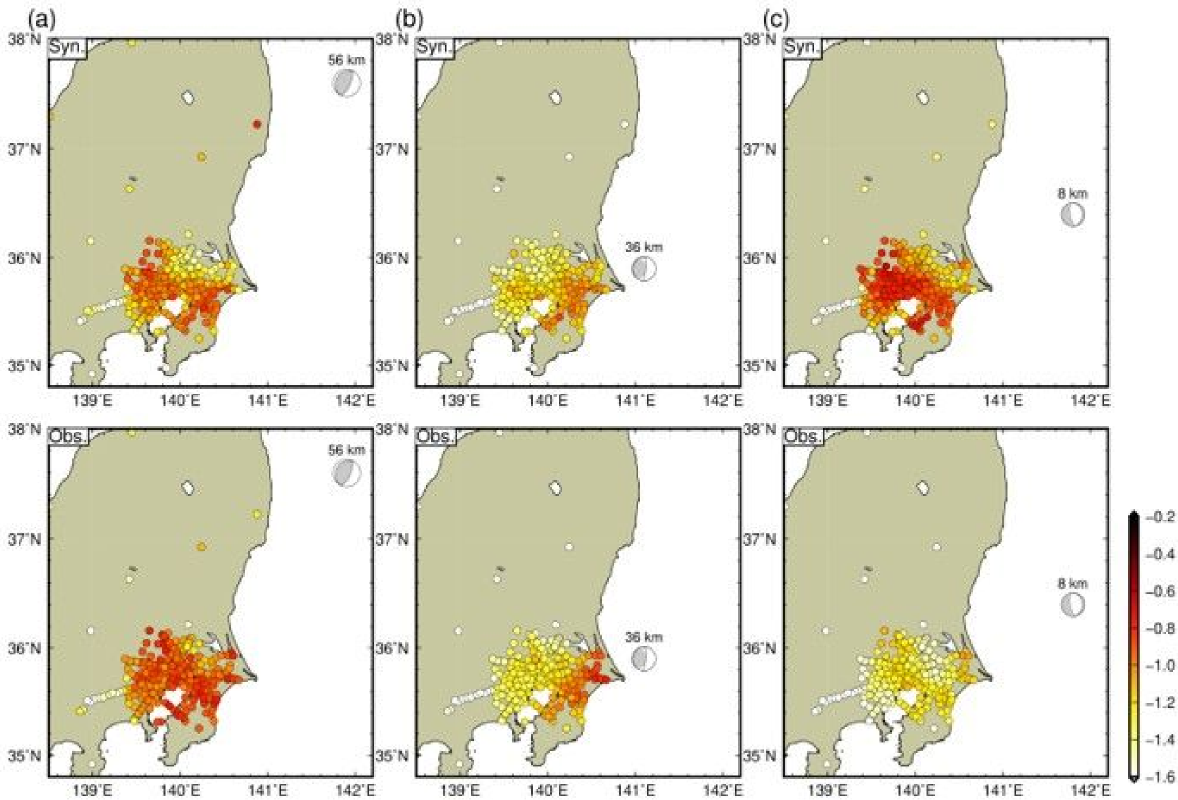

Figure 9

Peak ground velocity (PGV) for periods of 5-30 s. (a) Event A occurred on August 4, 2019, (b) Event B occurred on January 3, 2020, and (c) Event C occurred on February 6, 2020. Detail source parameters are described in Events A–C of Table 3. The top and bottom panels are the synthetic and observed PGVs, respectively. PGVs were evaluated by calculating the vector sum of three-component filtered seismograms at the F-net and MeSO-net stations. Plotted focal mechanisms are the optimal solutions of the 3D CMT inversions for the corresponding events. The JIVSM bedrock depths are illustrated in Figures 1, 7, and 9–11.

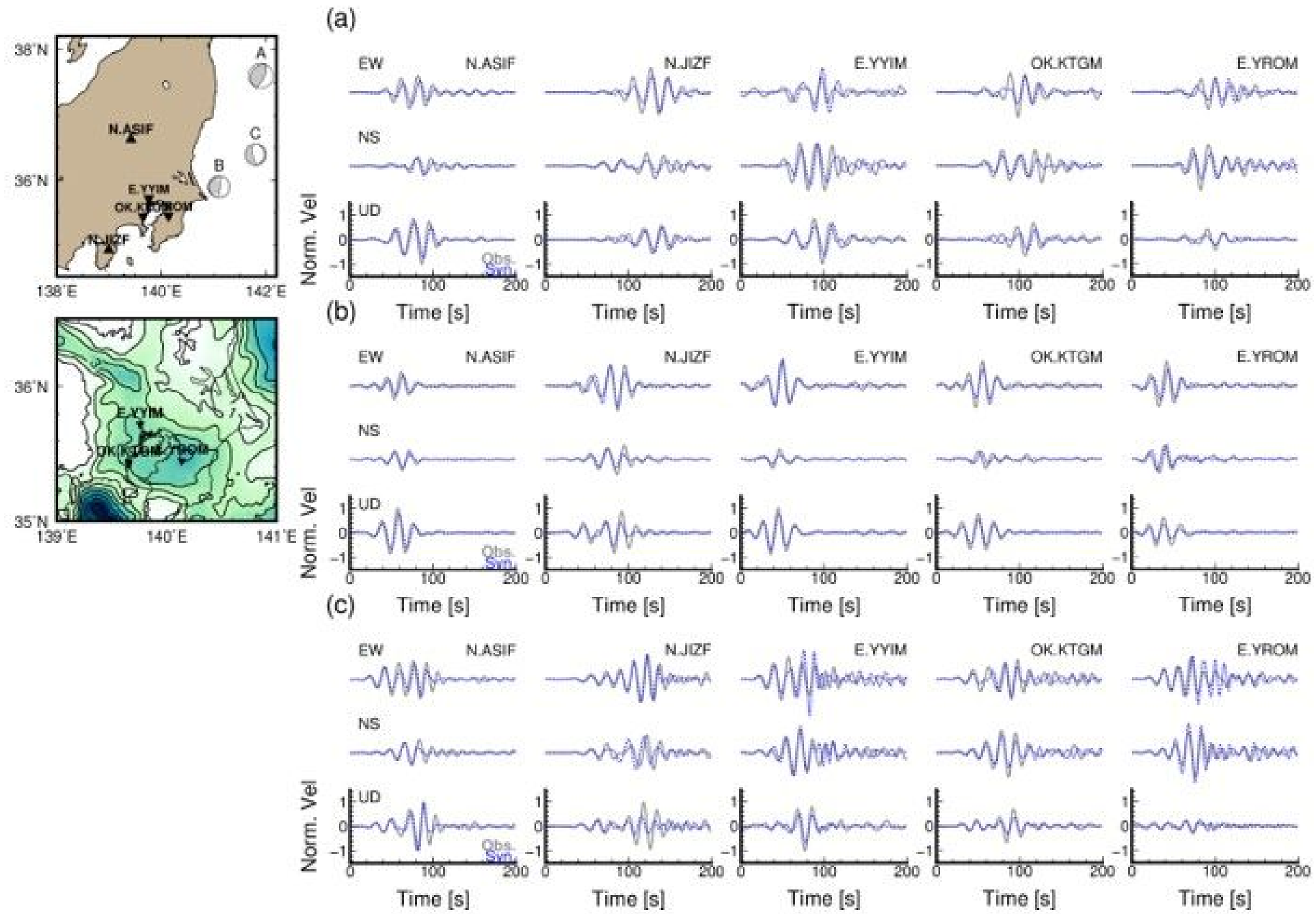

Figure 10

Comparisons between observed and simulated seismograms for periods of 15–30 s. We selected two F-net (N.ASIF and N.JIZF) and three MeSO-net (E.YYIM, OK.KTGM, and E.YROM) stations. Amplitudes at each station were normalized by the maximum amplitudes of observed seismograms for the periods of 15–30 s at each station. (a) Event A, (b) Event B, and (c) Event C. Gray and blue dotted lines are the observed and simulated seismograms, respectively. Left panels show used stations and bedrock depths of the JIVSM. Colors for bedrock depths are similar to Figure 1.

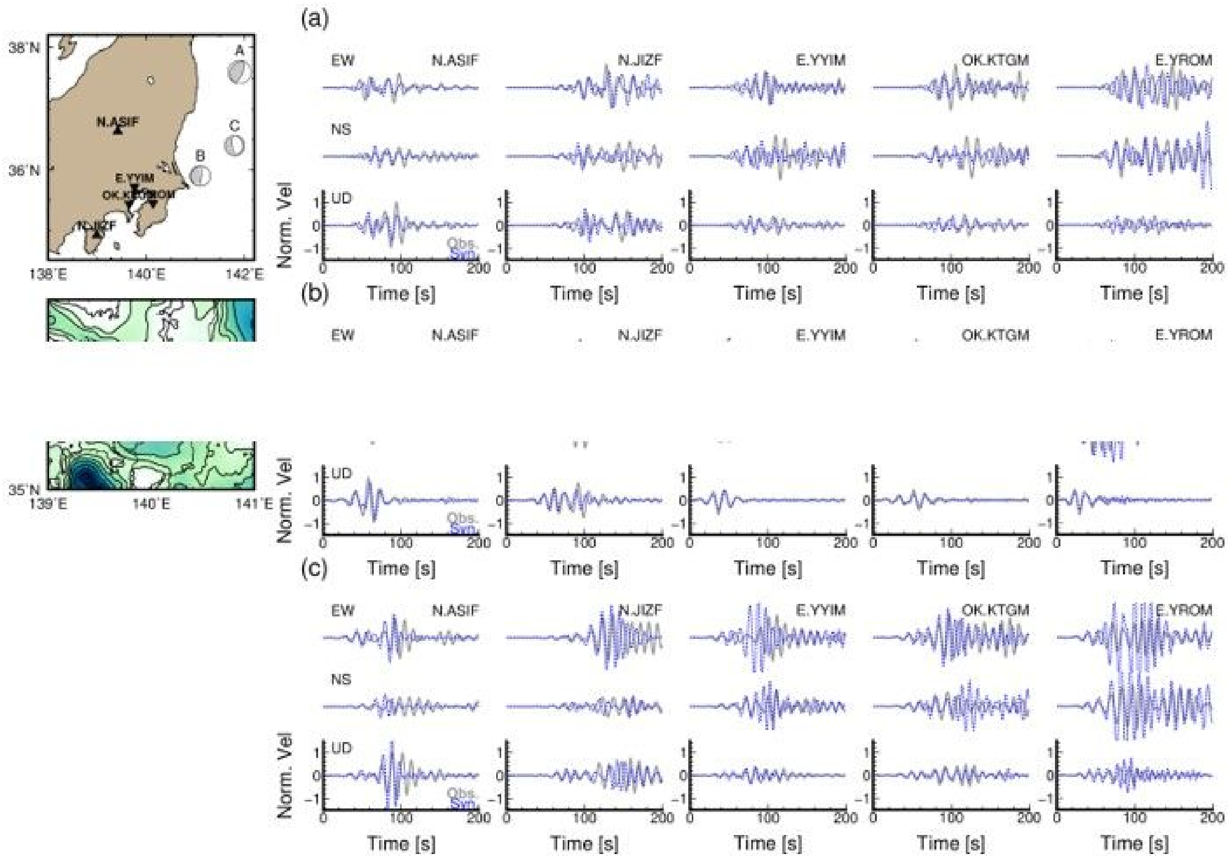

Figure 11

Comparisons between observed and simulated seismograms for periods of 10–20 s. We selected two F-net (N.ASIF and N.JIZF) and three MeSO-net (E.YYIM, OK.KTGM, and E.YROM) stations. Amplitudes at each station were normalized by the maximum amplitudes of observed seismograms for the periods of 10–20 s at each station. (a) Event A, (b) Event B, and (c) Event C. Gray and blue dotted lines are the observed and simulated seismograms, respectively. Left panels show used stations and bedrock depths of the JIVSM. Colors for bedrock depths are similar to Figure 1.

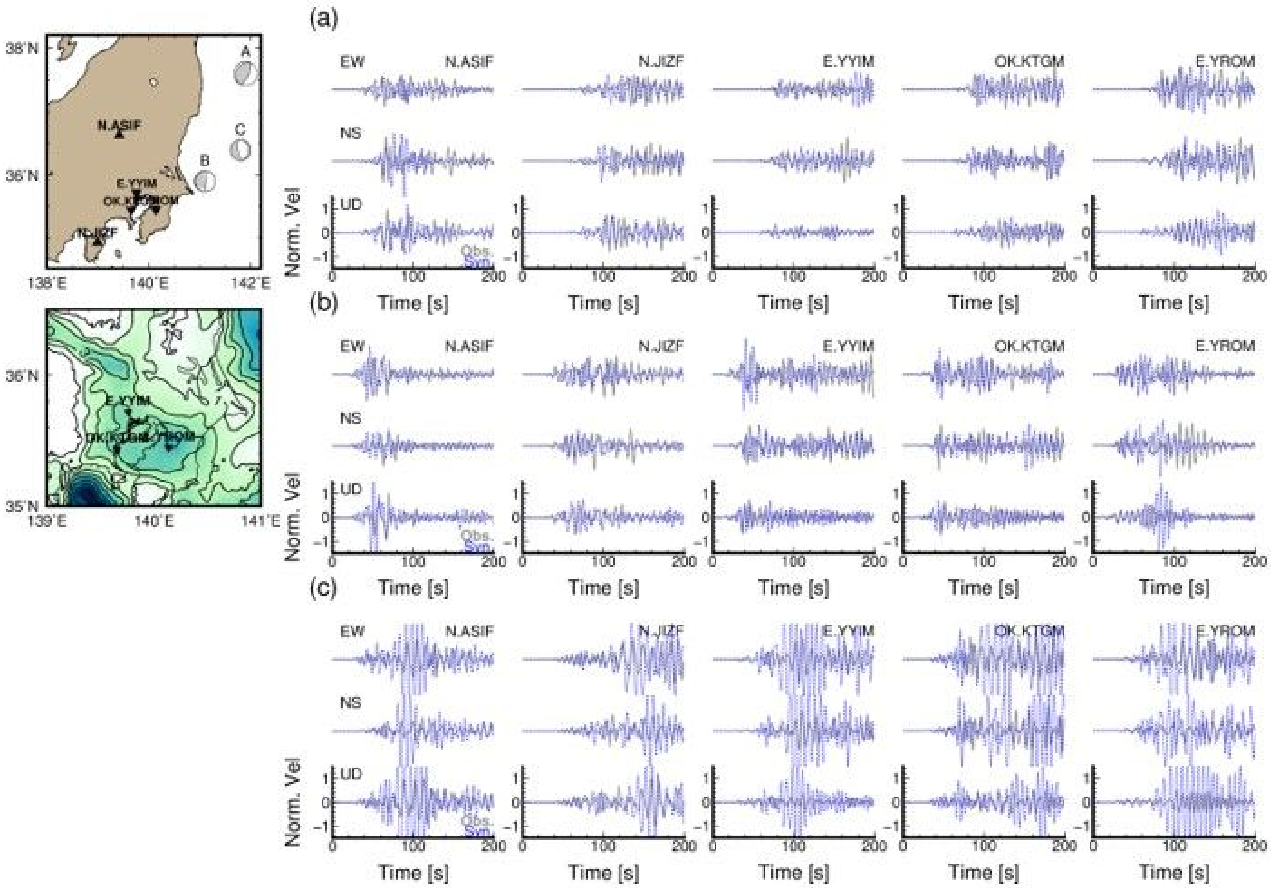

Figure 12

Comparisons between observed and simulated seismograms for periods of 5—16 s. We selected two F-net (N.ASIF and N.JIZF) and three MeSO-net (E.YYIM, OK.KTGM, and E.YROM) stations. Amplitudes at each station were normalized by the maximum amplitudes of observed seismograms for the periods of 5–16 s at each station. (a) Event A, (b) Event B, and (c) Event C. Gray and blue dotted lines are the observed and simulated seismograms, respectively. Left panels show used stations and bedrock depths of the JIVSM. Colors for bedrock depths are similar to Figure 1.

Supplementary Files

This is a list of supplementary files associated with this preprint. Click to download.

- Graphicalasbtract.png
- 2020TakemuraYoshimotoShiomiEPSSI.docx